PNAS
www.pnas.org

Supplementary Information for

Structural insights into unique features of the human mitochondrial ribosome recycling

Ravi K. Koripella[1], Manjuli R. Sharma[1], Paul Risteff[1], Pooja Keshavan[1], and Rajendra K. Agrawal[1,2*]

Rajendra K. Agrawal
Email: e-mail: rajendra.agrawal@health.ny.gov
Tel: (518) 486 5797

This PDF file includes:

Supplementary text
Figs. S1 to S8
Tables S1
References for SI reference citations

Supplementary Information Text

Materials and Methods:

Isolation of mitochondria from HEK cells:

The source of mitochondrial ribosomes was human embryonic kidney cells lacking N-acetyl-glucosaminyltransferase I (HEK293S GnTI) that were cultured in roller bottles using FreeStyle™293 media (Gibco, Life Technologies) supplemented with 5% fetal bovine serum (Gibco, Life Technologies). After centrifugation at 1,000 x g for 7 minutes, the HEK293S GnTI cell-pellet was transferred to a glass homogenizer and resuspended in buffer containing 50 mM HEPES-KOH pH 7.5, 10 mM KCL, 1.5 mM MgOAc, 70 mM sucrose, 210 mM mannitol, 1 mM EDTA, 1 mM EGTA, 1 mM DTT, and 1 mM PMSF. The cells were homogenized by applying 120 strokes and the supernatant was separated from the cell debris by spinning at 950 x g for 15 minutes. The supernatant was then spun at 11,000 x g for 15 minutes, and the resulting pellet that contains crude mitochondria was resuspended in SEM buffer (250 mM sucrose, 20 mM HEPES-KOH pH 7.5, 1 mM EDTA, and 1 mM EGTA). RNase-free DNase I (3 units /ml) was added to the crude mitochondria and incubated at 4°C for 1 hour in a rocking platform to allow gentle mixing. A discontinuous gradient was prepared in a Beckman polyallomer tube by layering 2.5 ml of 60 %, 4 ml of 32 %, 1 ml of 23 %, and 1 ml of 15 % sucrose solutions in buffer containing 10 mM HEPES-KOH pH 7.5 and1 mM EDTA. DNase-treated sample was loaded on the discontinuous gradient and centrifuged for one hour at 135,000 x g using Ti70 rotor in Beckman ultracentrifuge. The brownish-orange layer containing pure mitochondria was carefully separated and re-suspended in SEM buffer. The sample was then spun at 10,000 x g for 15 minutes, and the pellet was stored at -80°C.

Isolation of mitoribosomes from mitochondria:

Four volumes of lysis buffer (25 mM HEPES-KOH pH 7.5, 100 mM KCl, 25 mM MgOAc, 1.7 % Triton X-100, 2 mM DTT and 1 mM PMSF) was added to the mitochondrial-pellet and then incubated for 15 minutes at 4°C. The sample was centrifuged at 30,000 x g for 20 minutes and the supernatant was loaded on top of 1 M sucrose cushion in buffer (20 mM HEPES-KOH pH 7.5, 100 mM KCl, 20 mM MgOAc, 1% Triton X-100 and 2 mM DTT). After centrifugation for 17 hours at 90,000 x g using Ti70 rotor in Beckman ultracentrifuge, a minimal volume of Mitobuffer (20 mM HEPES-KOH pH 7.5, 100 mM KCl, 20 mM MgOAc, and 2 mM DTT) enough to dissolve the pellet was added. 10 – 30 % continuous sucrose density gradients were prepared in Mitobuffer, using the gradient making apparatus (C.B.S. Scientific Co.). The resuspended pellet was subjected to 10 – 30 % continuous sucrose density gradient centrifugation at 60,000 x g for 17 hours using Sw32 rotor in Beckman ultracentrifuge. The gradient was fractionated on ISCO gradient analyzer (Teledyne ISCO, Inc), and the fractions corresponding to the mitoribosomes were collected and pooled. Finally, the pooled mitoribosomes were concentrated by spinning them at 130,000 x g for 6 hours using Ti70 rotor, and the pellet was resuspended in Polymix buffer (5 mM HEPES-KOH pH 7.5, 100 mM KCl, 20 mM MgOAc, 5 mM NH_4Cl, 0.5 mM $CaCl_2$, 1 mM DTT, 1 mM spermidine, and 8 mM putrescine).

Purification of RRF_{mt}:

RRF_{mt} clone was a gift from Prof. Linda Spremulli, University of North Carolina. The SUMO-tagged RRF_{mt} was over-expressed in Rosetta2 cell lines and lysis buffer (500 mM NaCl, 1X PBS, 4 mM ß-mercaptoethanol, 1 mM PMSF, and 10 mM imidazole) was added to the pelleted cells. After sonication, the lysate was treated with DNase and then centrifuged for 30 minutes at 16,000 x g. The supernatant was applied to a His-trap Ni^{2+} column and the SUMO-tagged protein was eluted from the column using elution buffer (250 mM NaCl, 1X PBS, 4 mM ß-mercaptoethanol, and 300 mM imidazole) using standard affinity purification protocols. The purified protein was dialyzed in buffer (20 mM Tris-HCl pH 8.0,

250 mM NaCl, 4 mM ß-mercaptoethanol, and 5% glycerol) and then the SUMO tag was cleaved from RRF$_{mt}$ by incubation with SUMO express protease for 1 hour at 30°C. Finally, the SUMO tag and the SUMO express protease were separated from the RRF$_{mt}$ by passing through a His-trap Ni^{2+} column that specifically adsorbs the SUMO tag and the SUMO express protease while pure RRF$_{mt}$ was released into the column flow-through.

Preparation of the 55S-RRF$_{mt}$ complex:

50 mM puromycin was added to 100 nM 55S mitochondrial ribosomes in Polymix buffer and incubated for 10 minutes at 37°C to release any P/P-state tRNAs from the large mitoribosomal subunit. This step was necessary to free up the anticipated RRF$_{mt}$ binding site on the mitoribosome. This step was followed by the addition of 10 μM RRF$_{mt}$ and an additional 5 minutes incubation at 37°C. The reaction mixture was then immediately utilized for grid preparation for cryo-EM analysis.

Cryo-electron microscopy:

Quantifoil holey copper 1.2/1.3 grids were pre-coated with a thin layer (~ 50 Å thick) of home-made continuous carbon film and glow-discharged for 30 seconds using a plasma sterilizer. 4 μl of the sample was applied to the grids, incubated for 15 seconds at 4°C and 100% humidity and then blotted for 4 seconds before flash-freezing into the liquid ethane using Vitrobot (FEI company). Data was acquired on a Titan Krios electron microscope (FEI company) equipped with a Gatan K2 summit direct-electron detecting camera at 300 KV. A defocus range of 1.0 to 3.0 μm was used at a calibrated magnification of 105,000 X, yielding a pixel size of 1.09 Å on the object scale. A dose rate of 7 electrons per pixel per second and an exposure time of 10 seconds resulted in a total dose of 70 eÅ^{-2}. After determining their contrast transfer function (CTF) parameters using CTFFIND4 (1), the bad micrographs were deselected from the good ones. The data was further processed in Relion 2.0 (2) and a total of 288,138 particles were picked from the selected 5,305 micrographs using the auto-pick function.

CryoSPARC (3) was used to perform all the subsequent 2D and 3D classifications and refinements. From 288,138 autopicked particles, 144,057 good particles were selected after reference-free 2D classification. Particles in the selected 2D averages were then subjected to an initial reference-based heterogeneous 3D classification that yielded four major 3D classes (Fig. S1). The Class I and the Class II turned out to be 55S ribosomes in their ratcheted and unratcheted conformational states, respectively. The Class I that contained 67,116 particles showed a strong density for the ligand RRF_{mt}, whereas the Class II contained 26,195 particles and did not have any density for RRF_{mt}. The Class III with 42,352 particles contained only the 39S mitoribosomal subunits, while Class IV with 8,394 particles was regarded as junk since it did not produce any defined structure. Class I, Class II and Class III were further refined to 3.9 Å, 4.4 Å and 4.3 Å resolution, respectively.

In order to better characterize the binding positions mitochondrial tRNAs, particles in classes I and II were independently subjected to focused classification after signal subtraction using Relion (2), and refined using cryo-SPARC (3) (Fig. S4).

Model building and refinement:

The model of the 55S mitoribosome was generated by using the previously published coordinates of human mitoribosome (4) (PDB ID: 3J9M) as a template. Coordinates of the 28S and 39S subunits were docked independently as rigid bodies into the corresponding cryo-EM densities using Chimera (5). The models were further real-space refined and validated in PHENIX (6) to obtain optimal fitting to our cryo-EM densities. Robetta server (7) was used for initial homology model prediction for the human RRF_{mt} sequence. Robetta generated five homology models. All five models were placed into the corresponding cryo-EM density as rigid bodies using Chimera 1.11 (5) and the model that has the best matching features with the cryo-EM density corresponding to RRF_{mt} in Complex I, which has the best resolved density for the mito-specific N-terminal extension (NTE), was selected. The crystal structure of 70S bound *T. thermophilus* RRF (8)

(PDB ID: 4V5A) was used as reference and regions in the RRF$_{mt}$ that are not fully accommodated into the cryo-EM density were modelled in Chimera 1.11 (5). In its homology models the NTE of Human RRF$_{mt}$ folds into four α-helices. The 21 aa segment contiguous with structurally conserved domain I carries one of these four NTE α-helices that was built *de novo*, based on the recognizable secondary structural elements (SSEs) and bulky side-chains of the amino acids in the cryo-EM map, using the "Build structure" function in Chimera 1.1 (5) and Coot (9). Finally, we used the "Real-space refinement" function in PHENIX for optimization of the model into the cryo-EM density and further validation of the model (6). The Molprobity score (10) for the RRF$_{mt}$ was 1.51 (95th percentile), with 97.8 % favored rotamers, while Ramachandran plot favored protein geometry was 87.13 %, with 2.48 outliers in the loop regions. Finally, the combined coordinates of whole 55S mitoribosome and RRF$_{mt}$ were real-space refined using PHENIX. The calculated FSC between the Class I cryo-EM map and atomic coordinates of 55S-RRF$_{mt}$ complex is shown in Fig. S5B. The overall statistics of EM reconstruction and molecular modeling is provided in Table S1.

Supplemental Results:

Structure of the first 1-59 aa of the NTE.
Density corresponding to the first 1-59 aa residues were not resolved in our map and was visible in the low-pass filtered map only at low threshold values, suggesting high flexibility of the RRF$_{mt}$'s N-terminus. Nevertheless, the low-pass filtered density allowed us to tentatively place three α-helices predicted in the homology model (Fig. S8). These placements suggest that NTE would run up to the α-sarcin/ricin loop region of the 16S rRNA. However, because of its limited resolution, we refrain from interpreting any molecular interaction of the first 59 aa segment with the mitoribosome.

Positions of mitochondrial tRNAs in RRF$_{mt}$-bound and unbound 55S ribosomes.

Our 55S-RRF$_{mt}$ complex carries the native, indigenously-bound mRNA and tRNAs. However, densities corresponding to both these ligands were relatively weak in both the RRF$_{mt}$-bound and unbound 55S ribosome maps, and were visible only at low threshold values, apparently due to averaging of multiple species of mitochondrial tRNAs present in the complex and mixing of tRNA unbound population of the mitoribosome. Furthermore, binding of tRNA in the E site region is expected to be inherently weak in mammalian mitoribosome due to loss of multiple rRNA segments that constitute the E site in cytoplasmic ribosomes. To extract information about the precise location of tRNAs in our maps, we subjected two major classes (Class I and Class II) to signal subtraction and focused classification and obtained five classes (Fig. S4) with varying extents of 28S subunit rotation and tRNA occupancy. Of these, the major class, referred to as Class III, showed RRF$_{mt}$ and a pe/E-state tRNA in mitoribosome with fully rotated 28S subunit. Class IV, represented by ~14 % of RRF$_{mt}$-bound original Class I, showed only fragmented RRF$_{mt}$ density, but in this case tRNA was observed in the E/E state with partially rotated 28S subunit.

Among three classes obtained from the original RRF$_{mt}$-unbound class (Class II), two major classes, Class V and Class VI, also carried a pe/E-state tRNA, without or with partial rotation of 28S subunit, suggesting that the existence of the pe/E state tRNA in mitoribosome is not related to the subunit rotation. The smallest of all classes, Class VII, showed a fragmented density for both the P/P- and pe/E-state tRNAs.
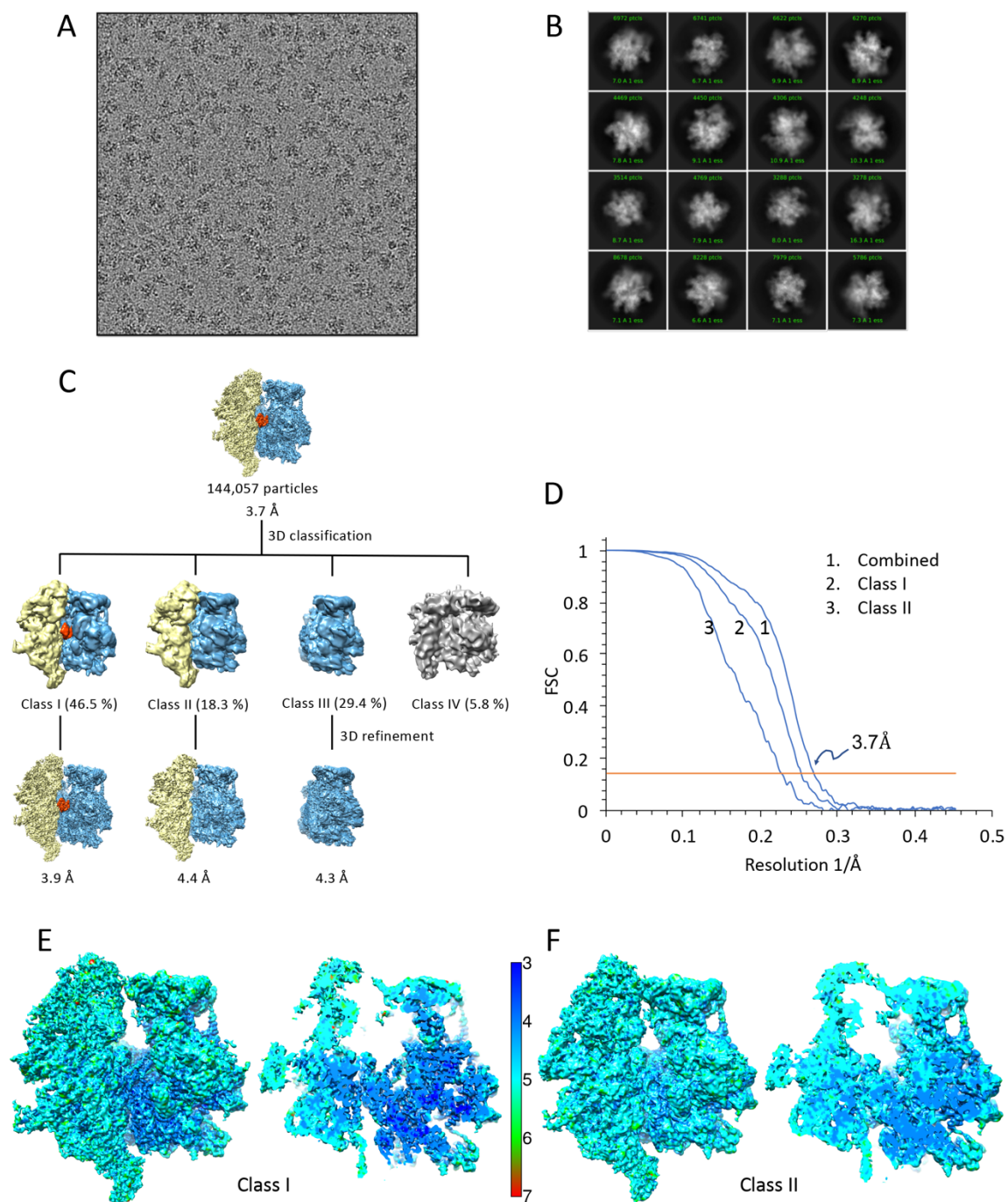
Fig. S1. Image processing of the 55S-RRF_mt complex. (A) A typical electron micrograph, showing the human 55S mitoribosome-RRF_mt complex. (B) Representative two-dimensional (2D) class averages used in three-dimensional (3D) reconstructions. (C) Flow-chart showing results of 3D classification and

refinements. A total of 144,057 particles corresponding to the selected 2D averages were refined to 3.7 Å. To remove conformational heterogeneity, the particles were subjected to 3D classification that yielded four different classes. After discarding the poorly aligned particles (Class IV), particles corresponding to the other three classes were independently refined, to 3.9 Å (Class I, with RRF_{mt}-bound 55S), 4.4 Å (Class II, empty 55S), and 4.3 Å (Class III, empty 39S). (D) Fourier-shell correlation (FSC) curves of the final three maps that were used in our analysis. Local resolution for refined (E) class I and (F) Class II. Right panels in both (E) and (F) show local resolution maps of the core regions after applying cutting planes.
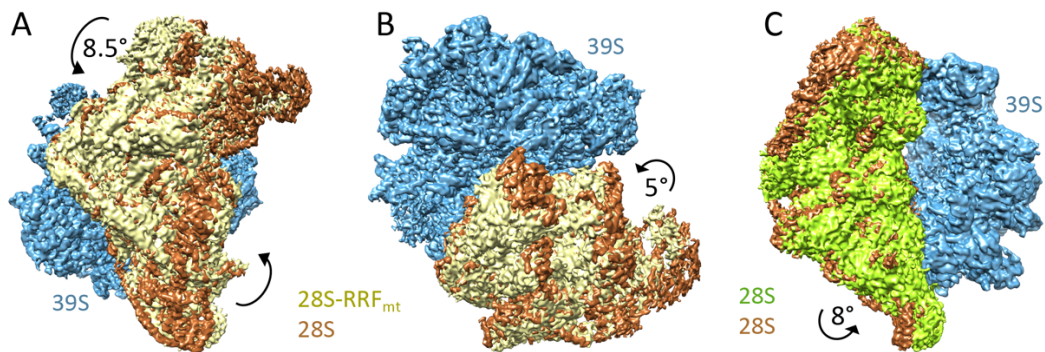
Fig. S2. Intersubunit movements and the 28S head rotation in RRF$_{mt}$-bound human 55S mitoribosome. (A) Superimposition of the cryo-EM maps of the RRF$_{mt}$-bound 55S mitoribosome (Class I) with that of an empty 55S mitoribosome (4) revealed an overall ~ 8.5 ° rotation of the 28S subunit (yellow) in an anti-clockwise direction relative to the 39S subunit (blue). (B) The anti-clockwise movement is accompanied by an additional ~ 5 ° rotation of the 28S head domain away from the 39S subunit. (C) Superimposition of the cryo-EM maps of the empty 55S mitoribosome (Class II from this study) with the published empty 55S mitoribosome (4) revealed an overall ~ 8 ° rotation of the shoulder side of the Class II 28S subunit (green) towards the 39S subunit (blue), a kin to "subunit rolling" (11) around a vertical axis. The 28S subunit of an empty mitoribosome from the previous study (4) is colored brown in all three panels.
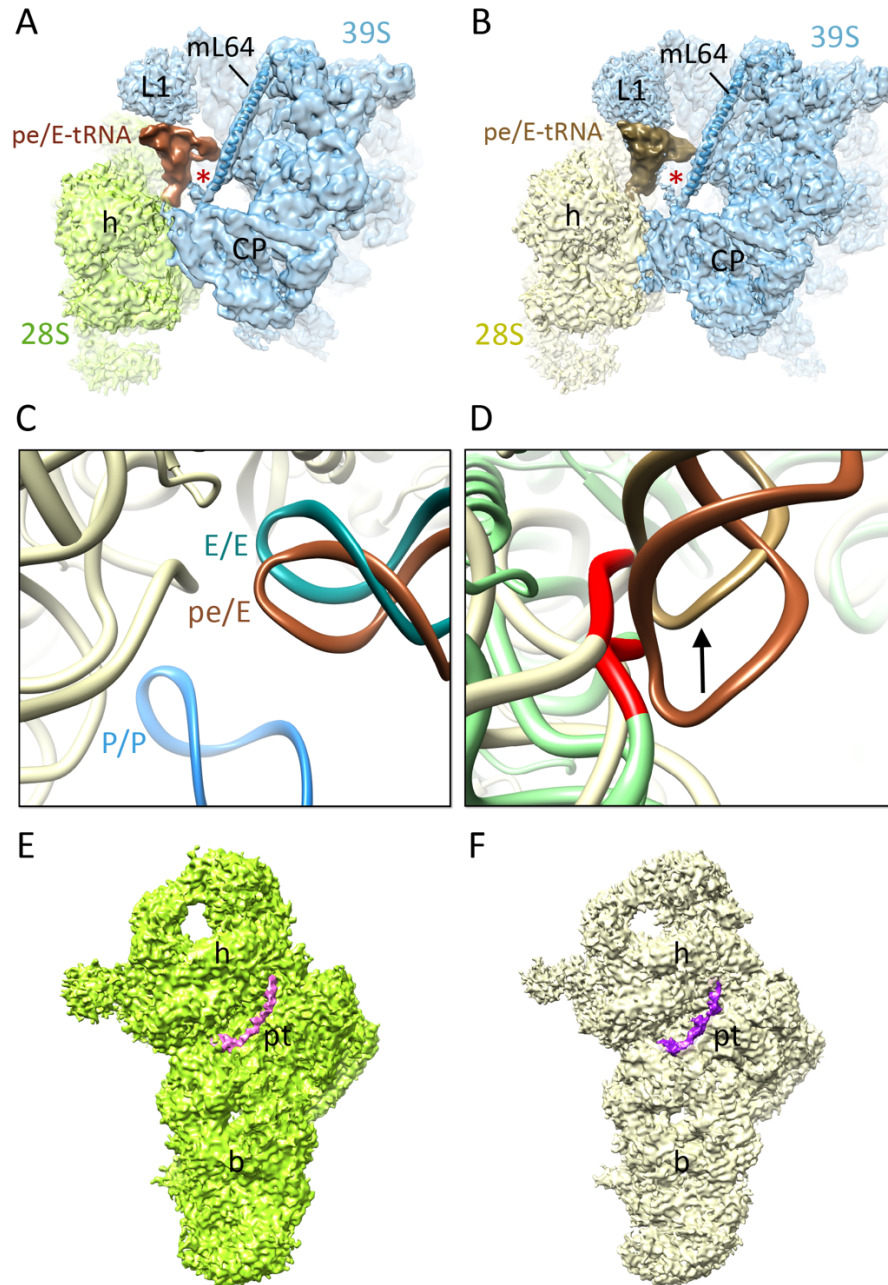
Fig. S3. Mito-specific interactions of the pe/E-state tRNA and presence of mRNA in the RRF$_{mt}$-bound and unbound 55S mitoribosomes. Location of the pe/E-tRNA (12) in (A) the RRF-free 55S ribosome (Class II), and (B) the RRF$_{mt}$-bound 55S ribosome (Class I). In both cases, a mito-specific interaction with a density corresponding to the C-terminus of mL64 is highlighted with a red asterisk (*). It should be noted that tRNA densities are weak in both complexes, but it allows us to place the tRNA model. (C) The relative positioning of pe/E

tRNA in our unrotated RRF$_{mt}$-unbound map as compared the P/P (13, 14) and E/E (4) tRNA states in the mitochondrial ribosomes. (D) Comparison of pe/E state tRNAs in our major RRF$_{mt}$ free (Class II, and its sub-class V, see Fig. S4) and RRF$_{mt}$-bound (Class I, and its sub-class III, see Fig. S4) classes. The arrow points to a clear shift in anticodon of the pe/E-tRNA, along with the shift in interacting 12S rRNA loop regions G1419-G1421 (red) between control (green) and RRF$_{mt}$-bound (pale yellow) maps. (E and F) Weak mass densities corresponding to indigenously bound mRNAs (pink and purple) in both Class II and Class I maps, respectively, could be observed.
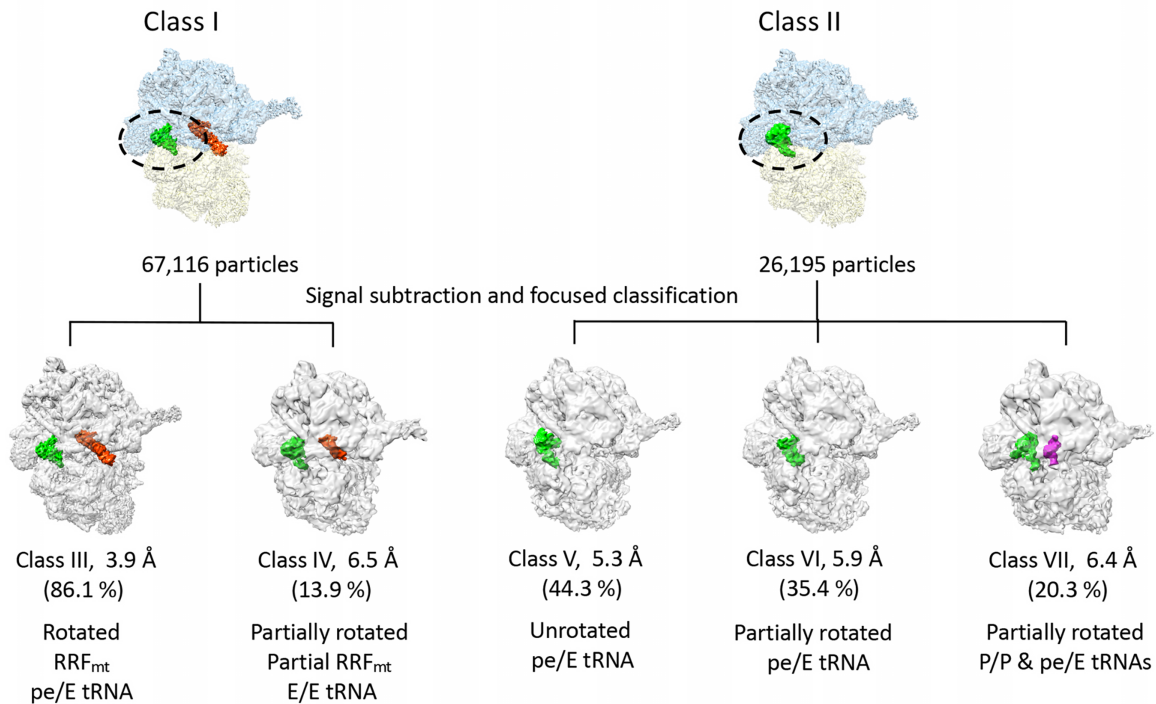
Fig. S4. Signal subtraction and focused classification of particles in Class I and Class II datasets. Both major classes (Class I and Class II, Fig. S1) were subjected to signal subtraction and focused classification. The resulting five classes revealed varying degrees of 28S subunit rotation, RRF_{mt} binding and multiple tRNA-binding states in the E-site region. The state and structure of tRNA and RRF_{mt} in Class III matched closely with that in its parent class I. Smallest of the classes, Class VII, also showed a density corresponding to the P/P-site tRNA.
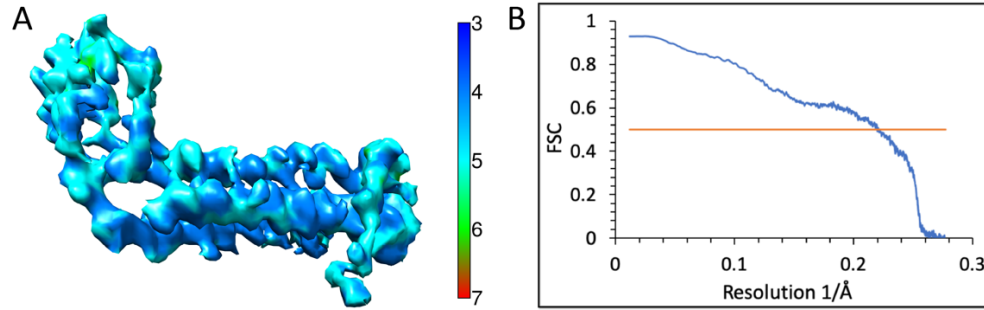
Fig. S5. Local resolution map of the RRF$_{mt}$, and map-model FSC. (A) Map showing the local resolution of RRF$_{mt}$ extracted from the refined Class I 55S-RRF$_{mt}$ complex, and (B) FSC between the Class I cryo-EM map and corresponding atomic coordinates.
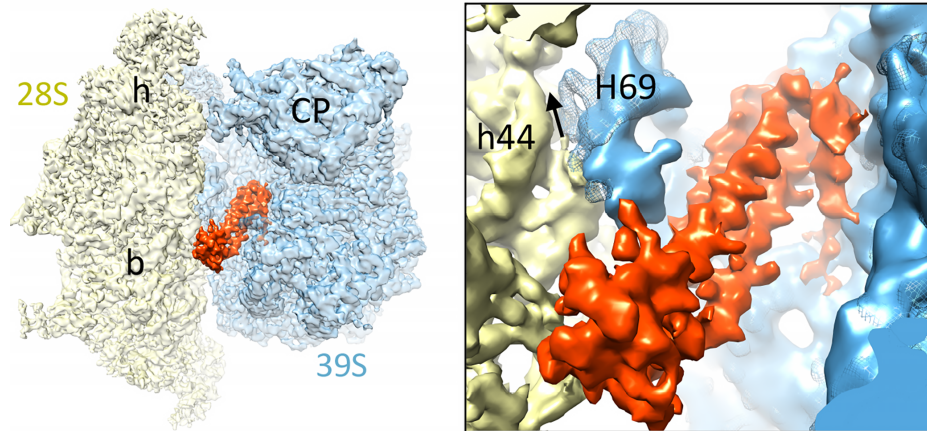
Fig. S6. Movement in the 16S rRNA helix 69 (bridge B2a) in the RRF$_{mt}$-bound map. The class I (39S subunit shown as mesh) and class II (39S shown as solid blue) maps are superimposed to reveal the movement (pointed by an arrow) in H69. RRF$_{mt}$ (orange) is also shown.

```
A  H.sapiens          MA-LGLKCF-RMVHPTFRNYLAASIRPVSEVTLKTVHERQH---GHRQYMAYSAVPVRHF   55
   P.aeruginosa        ------------------------------------------------------------    0
   E.coli              ------------------------------------------------------------    0
   S.typhimurium       ------------------------------------------------------------    0
   T.maritima          ------------------------------------------------------------    0
   T.thermophilus      ------------------------------------------------------------    0
   S.oleracea          MAASSLSSATSYLHSFRRRNSCVSLQGVSDMECNIARTNVSVWRSSANYVRM-DCGVKKF   59
   M.tuberculosis      ------------------------------------------------------------    0
   M.smegmatis         ------------------------------------------------------------    0
   C.botulinum         ------------------------------------------------------------    0
   C.tetani            ------------------------------------------------------------    0
   L.monocytogenes     ------------------------------------------------------------    0
   S.aureus            ------------------------------------------------------------    0
   S.pyogenes          ------------------------------------------------------------    0


   H.sapiens          ATKKAKAKG----KGQS-QTRVNINAALVEDIINLEEVNEEMKSVIEALKDNFNKTLNIR  110
   P.aeruginosa        -------------------------MINEI--KKEAQERMGKTLEALGHAFAKIRTGR    31
   E.coli              -------------------------MISDI--RKDAEVRMDKCVEAFKTQISKIRTGR    31
   S.typhimurium       -------------------------MISDI--RKDAEARMEKCVEAFKTQISKVRTGR    31
   T.maritima          -------------------------MVNPF--IKEAKEKMKRTLEKIEDELRKMRTGK    31
   T.thermophilus      -------------------------MTLKEL--YAETRSHMQKSLEVLEHNLAGLRTGR    32
   S.oleracea          SGKAVVVKQLQNRAGTFRCATMEEVEAEKSLI--ETNTKQRMEKTIETIRSNFNSVRTNR  117
   M.tuberculosis      -------------------------MIDEA--LFDAEEKMEKAVAVARDDLSTIRTGR    31
   M.smegmatis         -------------------------MIDET--LFDAEEKMEKAVSVARDELGSIRTGR    31
   C.botulinum         -------------------------MIKDI--IKNAEEKMQKTVTVLKSELGTMKAGR    31
   C.tetani            -------------------------MLKEI--MNTAEDKMSKALLALKKDLASLKAGR    31
   L.monocytogenes     -------------------------MSKEV--LSKSKEKMEKAEQALTRQLGTIRAGR    31
   S.aureus            ------------------------MSDI--INETKSRMQKSIESLSRELANISAGR    30
   S.pyogenes          -------------------------MANAI--IETAKERFAQSHQSLSREYASIRAGR    31
```
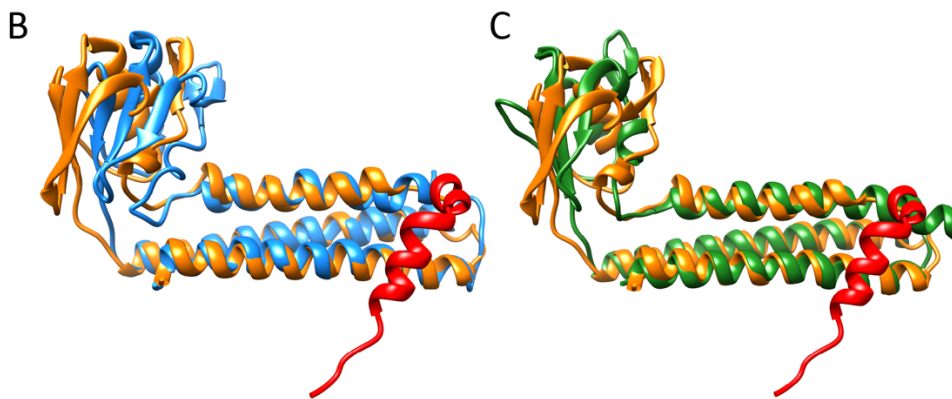
Fig. S7. Comparison of RRF$_{mt}$ with bacterial and chloroplast homologues.
(A) Sequence alignment of RRF$_{mt}$ with RRFs from various bacterial species and chloroplast. The mito- and chloro-specific NTEs are highlighted in red and green, respectively. Structural comparisons of the human 55S mitoribosome-bound RRF$_{mt}$ with the 70S ribosome-bound (B) bacterial (blue) (8) (PDB ID 4V5A) and (C) chloroplast (15) (PDB ID 6ERI) RRFs. In all three structures the orientation of domain I is very similar, however, domain II adopts different conformations. The NTE of RRF$_{mt}$ is highlighted in red, whereas structure for the NTE of chloroplast RRF is unknown.
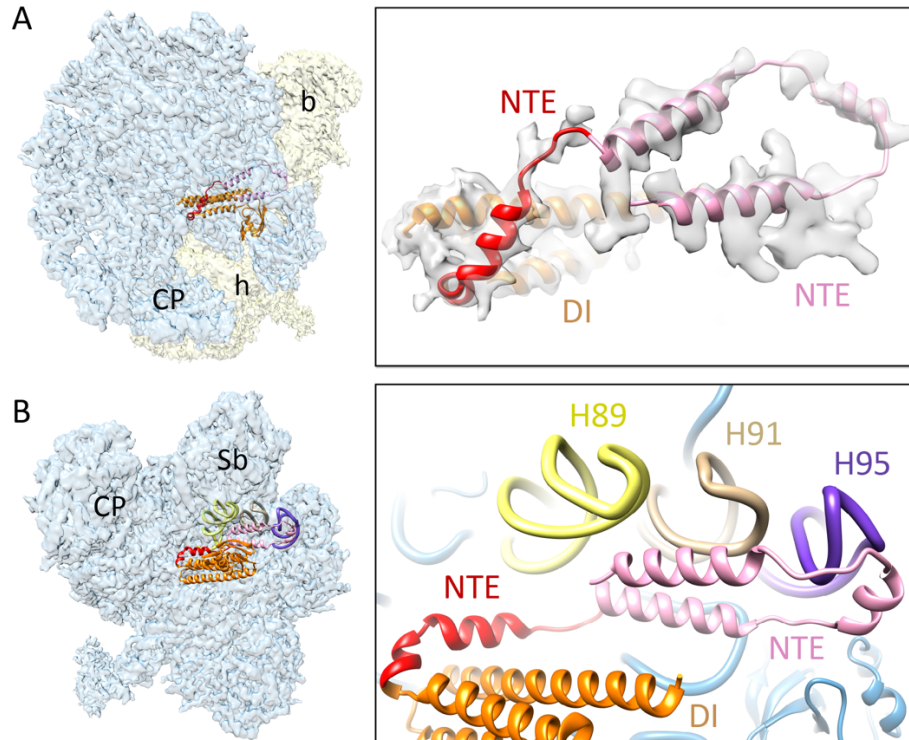
Fig. S8. Structure of the first 1-59 aa of the NTE. (A) Low pass-filtered density corresponding to the first 1-59 aa residues extracted from the RRF$_{mt}$-bound 55S complex (Class I). Part of the NTE that could be modelled *de novo* is shown in red, and a tentative model for the remaining 59 aa is shown in pink. (B) Position of the first 1-59 aa residues relative to 16S rRNA helices of the 39S subunit, including H89, H91 and H95 (α-sarcin/ricin loop). Thumbnails to left depict overall orientations of the (A) 55S mitoribosome and (B) 39S subunit, with semitransparent 28S (yellow) and 39S (blue) subunits, and overlaid positions of ligands. Landmarks on the thumbnail: h, head, and b, body of the 28S subunit, and CP, central protuberance and Sb, L11 stalk base of the 39S subunit.

Table S1. Data Collection, Refinement and Model Validation

Description	55S-RRF$_{mt}$ (Class I)	55S (no RRF$_{mt}$) (Class II)
Data collection and Refinement		
Microscope	FEI Titan Krios	
Voltage (kV)	300	
Pixel size (Å)	1.09	
Defocus range (μm)	1.0 to 3.0	
Average e$^-$ dose per image (e$^-$/Å^2)	69.5	
Software	RELION and cryoSPARC	
Particles (initial)	144,057	
Particles (final)	67,116	26,195
Symmetry	C1	C1
FSC-threshold	0.143	0.143
Resolution (Å)	3.9	4.4
Map-sharpening B factor (Å^2) overall	- 107.6	- 88.8
RMS deviations		
Bonds lengths (Å)	0.001	0.002
Bonds angles (°)	0.365	0.452
Molprobity clashscore	1.91 (80th)	1.87 (82nd)
Clashscore, all atoms	4.91 (94th)	4.23 (96th)
Rotamer outliers (%)	0.63	0.32
Ramachandran plot		
Favored (%)	85.23	84.91
Outliers (%)	2.53	2.81
RNA		
Correct sugar puckers (%)	98.41	98.25
Angle outliers (%)	0.00	0.00
Bond outliers (%)	0.00	0.00
Good backbone conformations (%)	70.44	70.36
Model composition		
RNA bases	2,453	2,453
Protein residues	13,110	12,902
Accession codes		
Cryo-EM maps	EMD-0514	EMD-0515
PDB ID	6NU2	6NU3

References:

1. Rohou A & Grigorieff N (2015) CTFFIND4: Fast and accurate defocus estimation from electron micrographs. *J Struct Biol* 192(2):216-221.
2. Scheres SH (2012) RELION: implementation of a Bayesian approach to cryo-EM structure determination. *J Struct Biol* 180(3):519-530.
3. Punjani A, Rubinstein JL, Fleet DJ, & Brubaker MA (2017) cryoSPARC: algorithms for rapid unsupervised cryo-EM structure determination. *Nat Methods* 14(3):290-296.
4. Amunts A, Brown A, Toots J, Scheres SHW, & Ramakrishnan V (2015) Ribosome. The structure of the human mitochondrial ribosome. *Science* 348(6230):95-98.
5. Pettersen EF*, et al.* (2004) UCSF Chimera--a visualization system for exploratory research and analysis. *J Comput Chem* 25(13):1605-1612.
6. Adams PD*, et al.* (2010) PHENIX: a comprehensive Python-based system for macromolecular structure solution. *Acta Crystallogr D Biol Crystallogr* 66(Pt 2):213-221.
7. Kim DE, Chivian D, & Baker D (2004) Protein structure prediction and analysis using the Robetta server. *Nucleic Acids Res* 32(Web Server issue):W526-531.
8. Weixlbaumer A*, et al.* (2007) Crystal structure of the ribosome recycling factor bound to the ribosome. *Nat Struct Mol Biol* 14(8):733-737.
9. Emsley P, Lohkamp B, Scott WG, & Cowtan K (2010) Features and development of Coot. *Acta Crystallogr D Biol Crystallogr* 66(Pt 4):486-501.
10. Chen VB*, et al.* (2010) MolProbity: all-atom structure validation for macromolecular crystallography. *Acta Crystallogr D Biol Crystallogr* 66(Pt 1):12-21.
11. Budkevich TV*, et al.* (2014) Regulation of the mammalian elongation cycle by subunit rolling: a eukaryotic-specific ribosome rearrangement. *Cell* 158(1):121-131.
12. Ratje AH*, et al.* (2010) Head swivel on the ribosome facilitates translocation by means of intra-subunit tRNA hybrid sites. *Nature* 468(7324):713-716.
13. Greber BJ*, et al.* (2015) Ribosome. The complete structure of the 55S mammalian mitochondrial ribosome. *Science* 348(6232):303-308.
14. Sharma MR*, et al.* (2003) Structure of the mammalian mitochondrial ribosome reveals an expanded functional role for its component proteins. *Cell* 115(1):97-108.
15. Boerema AP*, et al.* (2018) Structure of the chloroplast ribosome with chl-RRF and hibernation-promoting factor. *Nat Plants* 4(4):212-217.